Two-photon polymerization based 4D printing of poly(N-isopropylacrylamide) hydrogel microarchitectures for reversible shape morphing

Yarali, Ebrahim; Mubeen, Ayman Ahmed; Cussen, Kai; van Zanten, Lennart; Moosabeiki, Vahid; Zadpoor, Amir A.; Accardo, Angelo; Mirzaali, Mohammad J.

DOI
10.1038/s41598-025-06269-2

Publication date
2025

Document Version
Final published version

Published in
Scientific Reports

Citation (APA)
Yarali, E., Mubeen, A. A., Cussen, K., van Zanten, L., Moosabeiki, V., Zadpoor, A. A., Accardo, A., & Mirzaali, M. J. (2025). Two-photon polymerization based 4D printing of poly(N-isopropylacrylamide) hydrogel microarchitectures for reversible shape morphing. *Scientific Reports*, *15*(1), Article 21549. https://doi.org/10.1038/s41598-025-06269-2

scientific reports

Check for updates

OPEN

Two-photon polymerization based 4D printing of poly(N-isopropylacrylamide) hydrogel microarchitectures for reversible shape morphing

Ebrahim Yarali[1,2]✉, Ayman Ahmed Mubeen[1], Kai Cussen[1], Lennart van Zanten[1], Vahid Moosabeiki[1], Amir A. Zadpoor[1], Angelo Accardo[2,3]✉ & Mohammad J. Mirzaali[1,3]✉

Incorporating shape-morphing capability into 3D microprinting enables the fabrication of 4D-printed microarchitectures as proof-of-concept actuators for potential use in soft robotics and microfluidic systems. The ability of these 3D microstructures to actuate rapidly and reversibly enables precise, non-invasive, and controllable deformation. In this study, we investigated the programmable shape-morphing behavior of 3D microarchitectures fabricated using two-photon polymerization (2PP) of a well-established temperature-responsive hydrogel, poly(N-isopropylacrylamide) (pNIPAM). We first systematically studied how 2PP 3D printing parameters (e.g., laser power, scanning speed) and the chemical composition of pNIPAM, including monomer and crosslinker, influence the shape morphing of bilayer microstructures within a temperature range of ~ 32 °C to 60 °C. The (thermo)mechanical properties of the hydrogels, including the Young's modulus, thermal expansion coefficients, and angular deflection, were also measured at different laser doses and temperatures. Based on these experimental measurements, we calibrated a thermomechanical model capable of predicting the shape morphing of 4D-printed microarchitectures. These microarchitectures served as proof-of-concept actuators, demonstrating the potential of programmable microscale soft robotics and microfluidic systems. The findings provide design guidelines for engineering stimuli-responsive 3D microstructures, highlighting limitations and opportunities for future integration into functional soft robotic or microfluidic systems made of a single material.

Keywords Temperature-responsive hydrogels, Two-photon polymerization, Shape morphing, 4D Microprinting, Soft actuators

Toward the fabrication of intelligent microfluidic systems and soft grippers with shape-morphing behavior, 4D printing offers a transformative approach by integrating stimuli-responsive materials with 3D printing technology[1,2]. The addition of time as the fourth dimension in 4D printing enables the creation of devices or structures that are programmed to change their shape or other properties, such as stiffness, in response to external stimuli[3].

To 4D print microarchitectures for various applications, such as soft robotics and microfluidics, several criteria are considered, depending on the intended use. Two general factors include *(i)* the material's compatibility with its surrounding environment (e.g., contact with biological tissues) and *(ii)* the nature of the external stimulus used to trigger shape morphing. Temperature-responsive 4D-printed structures, for example, are valued for their straightforward actuation mechanism and controllable response, though their actuation temperatures must suit the target application. In soft robotics, reversibility is an additional function that is often essential for

[1]Department of Biomechanical Engineering, Faculty of Mechanical Engineering, Delft University of Technology, Mekelweg 2, Delft 2628 CD, The Netherlands. [2]Department of Precision and Microsystems Engineering, Faculty of Mechanical Engineering, Delft University of Technology, Mekelweg 2, Delft 2628 CD, The Netherlands. [3]These authors jointly supervised this work: Mohammad J. Mirzaali and Angelo Accardo. ✉email: E.yarali@tudelft.nl; A.Accardo@tudelft.nl; M.J.Mirzaali@tudelft.nl

structures undergoing multiple shape morphing cycles. Additionally, multiscale applicability, from nanoscale to microscale, is critical for deployable actuators in confined environments, such as microfluidic systems.

One microfabrication technique that enables the precise creation of such temperature-responsive 3D microstructures is two-photon polymerization (2PP) direct laser writing[4–6]. 2PP offers submicrometer resolution by simultaneously absorbing two photons in a photoresist to initiate the polymerization reaction[7]. This capability makes it especially suited for creating programmable, reversible shape-morphing microstructures at the microscale, with potential use in soft robotics and temperature-responsive valves in microfluidic systems.

Among smart materials, such as shape memory polymers[8,9], shape memory alloys[10], shape memory ceramics[11,12], liquid crystalline polymers[13], and hydrogels[14,15], poly(N-isopropyl acrylamide) (pNIPAM)-based hydrogels[2,4,16] are particularly promising for 2PP 3D printing of soft actuators. These hydrogels exhibit hydrophilic behavior at room temperature due to hydrogen bonding between the polymer chains and water molecules. When the temperature increases beyond the lower critical solution temperature (LCST) of NIPAM (~ 32–35 °C[17–19]), the polymer chains rapidly transition from hydrophilic to hydrophobic, resulting in a significant (and reversible) volume change and dramatic shrinkage[20,21] (Fig. 1a). This temperature-responsive shape morphing makes pNIPAM hydrogels well-suited for soft robotic actuators and microfluidic applications.

Achieving controlled and predictable shape morphing in 4D-printed structures requires high tunability of the material's properties. pNIPAM offers this through adjustments in its chemical composition (e.g., monomer or crosslinker concentrations) and 3D printing parameters (e.g., laser power and scanning speed, Figs. 1a and c), in addition to temperature[4]. Such tunability in material properties can be rationally engineered to induce shape-morphing behavior, such as bending and twisting, in single-material structures. This is mainly attributed to the effect of mechanical heterogeneity or thermomechanical anisotropy induced within the design[3,4,22–26]. Such heterogeneity in the case of pNIPAM can be formed through spatially varying crosslinking density. This is commonly achieved using a bilayer beam configuration, where each layer is 3D printed with distinct parameters

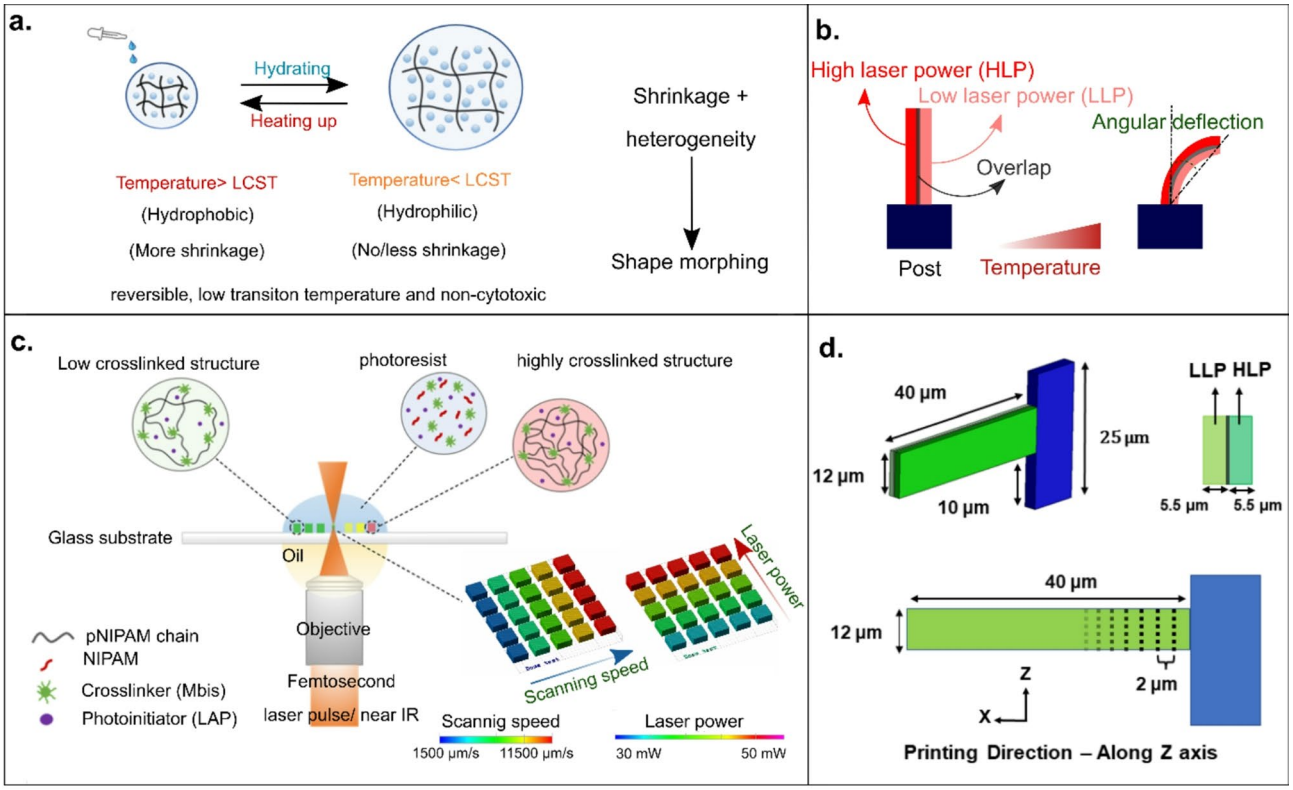

Fig. 1. **(a)** A schematic drawing illustrating the molecular mechanism of the pNIPAM when temperature exceeds lower critical solution temperature (LCST). A reversible transition between hydrophilic and hydrophobic states makes the hydrogel responsive to temperature. It also indicates that sophisticated shape morphing can be achieved if the deformation is heterogeneous. **(b)** A schematic drawing showing the bending of a 4D-printed bilayer beam from a single material (i.e., pNIPAM) and its angular deflection. The red, light red and gray layers represent the high laser power (i.e., HLP) dose, low laser power (i.e., LLP) dose and overlap. The dark blue object indicates the post, which is 3D printed with a very high dose to avoid deformation. **(c)** The 2PP 4D printing setup for creating pNIPAM-based microstructures. The microstructures are 3D printed through oil configuration with varying laser power and scanning speed. **(d)** The geometrical configuration of the bilayer beam. The beams were discretized into smaller slices along the *X* direction, and the print was performed in each slice along the *Z* direction to increase the mechanical stability. Note that the configuration of the bilayer beams was adapted from[4].

(e.g., laser power or scanning speed)[4], in addition to varying the chemical compositions within the layers. As temperature rises, differences in thermal expansion coefficients or volume changes between the layers cause the beam to bend, assuming strong interlayer bonding. Alternatively, incorporating a second material, such as particles or fibers, can enhance anisotropy and enable more complex deformations[27].

To date, 2PP 4D printing of pNIPAM has been explored for microscale shape-morphing applications, including simple beam bending[4,28], grippers, microarchitectures[29–31], and microfluidic systems[32]. These applications primarily rely on adjusting 3D printing parameters and incorporating stimuli-responsive modifications (e.g., Fe_3O_4 particles for NIR light responsiveness[30]). However, designing microarchitectures with controlled and predictable shape morphing, such as for microfluidic actuation, requires a deeper understanding of how 2PP 3D printing parameters and pNIPAM's thermomechanical properties interact.

Thus, this study focuses on thermomechanically characterizing 2PP 3D printed pNIPAM hydrogels, using nanoindentation to measure Young's modulus and assess strain rate effects, alongside measuring thermal expansion coefficients. We systematically investigate how 3D printing parameters (e.g., laser power, scanning speed, and hatching angle) and pNIPAM's chemical composition influence shape-morphing behavior in bilayer beams. A straightforward finite element model (FEM), calibrated and validated with experimental data, is developed to predict and control shape morphing of 3D microarchitectures. Finally, we demonstrate programmable deformation in proof-of-concept applications, including soft grippers and microfluidic systems, highlighting the potential of this approach for future smart systems.

Results and discussion

To elucidate the effect of intentional heterogeneity in single-material 2PP printed microstructures, we employed a bilayer design, where each layer exhibited a different thermomechanical property. This was achieved by polymerizing the layers using varying doses of laser energy, specifically different laser powers and scanning speeds (Fig. 1a and b). It is important to note that all the microarchitectures were 4D printed using this bilayer beam concept, with one layer referred to as the high laser power (HLP) layer and the other as the low laser power (LLP) layer. When the temperature of the bilayer beams dipped in water increases, the microstructures morph. To quantify the shape morphing of the beams, we measured the angular deflection on the beams after the temperature increases. Moreover, we performed all the experiments within a short-term period. Therefore, the long-term stability of this heterogeneity, particularly under repeated actuation and hydration/dehydration cycles, requires further investigation. It should also be noted that in our study, the configuration and initial dimensions of the bilayer beams were adapted from Hippler et al.[4].

Tuning the 2PP parameters to 3D print the bilayer beams

To fabricate mechanically stable bilayer beams via 2PP, we identified an optimal parameter range for laser power and scanning speed through a dose test study on an array of blocks made from pNIPAM (11 ×11 arrays) as shown in Figure S1 of the supplementary document, highlighted in light blue. The viable range for laser power was 76–100% (38–50 mW, relative to the maximum 50 mW), and for scanning speed, 6000–11,500 μm/s. At scanning speeds below 6000 μm/s or laser powers above 75% with low scanning speeds, the photoresist overheated, forming bubbles and compromising printability. On the other hand, higher scanning speeds (i.e., $\geq$ 6000 $\mu\, m/s$) combined with laser powers of 76–100% produced robust, and solid blocks. The selection criteria for these parameters prioritized printability (absence of burning) and overall shrinkage, assessed via structural integrity and dimensional stability after the print. For instance, 3D printed-blocks at 76% laser power and high scanning speeds ($\geq$ 6000 $\mu\, m/s$) exhibited greater shrinkage compared to those at 100% laser power, reflecting variations in crosslinking density that influence the Young's modulus and shrinkage of the material.

Nevertheless, achieving mechanical stability in bilayer beams after post-chemical development (see "Materials and methods") presents additional challenges, particularly for high-aspect-ratio bilayer beams. Unlike the dose test blocks, beams are 3D printed within the pNIPAM photoresist without direct adhesion to the glass substrate, increasing the chance to collapse if parameters are suboptimal. To address this, systematic tuning of the LLP and HLP layers doses was necessary to balance structural robustness with shape-morphing capability. It should also be noted that there was a pre-deflection in the 3D printed beams in some cases (Fig. 2a) due to the post-chemical development process of the pNIPAM in which the specimens were transformed from ethylene glycol to water[4]. Nevertheless, this pre-deflection vanished after one cycle when the microarchitectures were reheated.

Effect of the laser power and scanning speed on angular Deflection of the bilayer beams

To elucidate the effects of energy dose (i.e., laser power and scanning speed) on the angular deflection of the bilayer beams, we independently varied these parameters and measured the resulting angular deflection. For the laser power study, we adjusted the laser power of the LLP layer from 76 to 100% (relative to the maximum 50 mW, i.e., 38–50 mW) while keeping the HLP layer at 100% and maintaining a constant scanning speed of 8000 μm/s for both layers (Fig. 2b). As the LLP laser power increased from 85 to 100%, the angular deflection decreased from 26° to 0°, representing a 100% reduction. This trend arises because the higher laser power of the LLP layer reduces the difference in crosslinking density between the LLP and HLP layers, leading to smaller disparities in thermal shrinkage and, consequently, diminished beam deflection. Note that laser powers below 85% for the LLP layer resulted in structural instability, causing beam collapse during post-chemical development process.

To examine the effect of scanning speed on shape morphing, we fixed the laser power of the HLP layer at 100% (= 50 mW) and the LLP layer at 85% (= 42.5 mW), where conditions yielding maximum angular deflection from the laser power study, and varied the scanning speed from 8000 μm/s to 9500 μm/s for the LLP layer (Fig. 2b). In contrast to laser power, scanning speed had a lower impact, increasing the angular deflection from 26° to 32°, a change of approximately 23%. This suggests that scanning speed exerts less influence on crosslinking

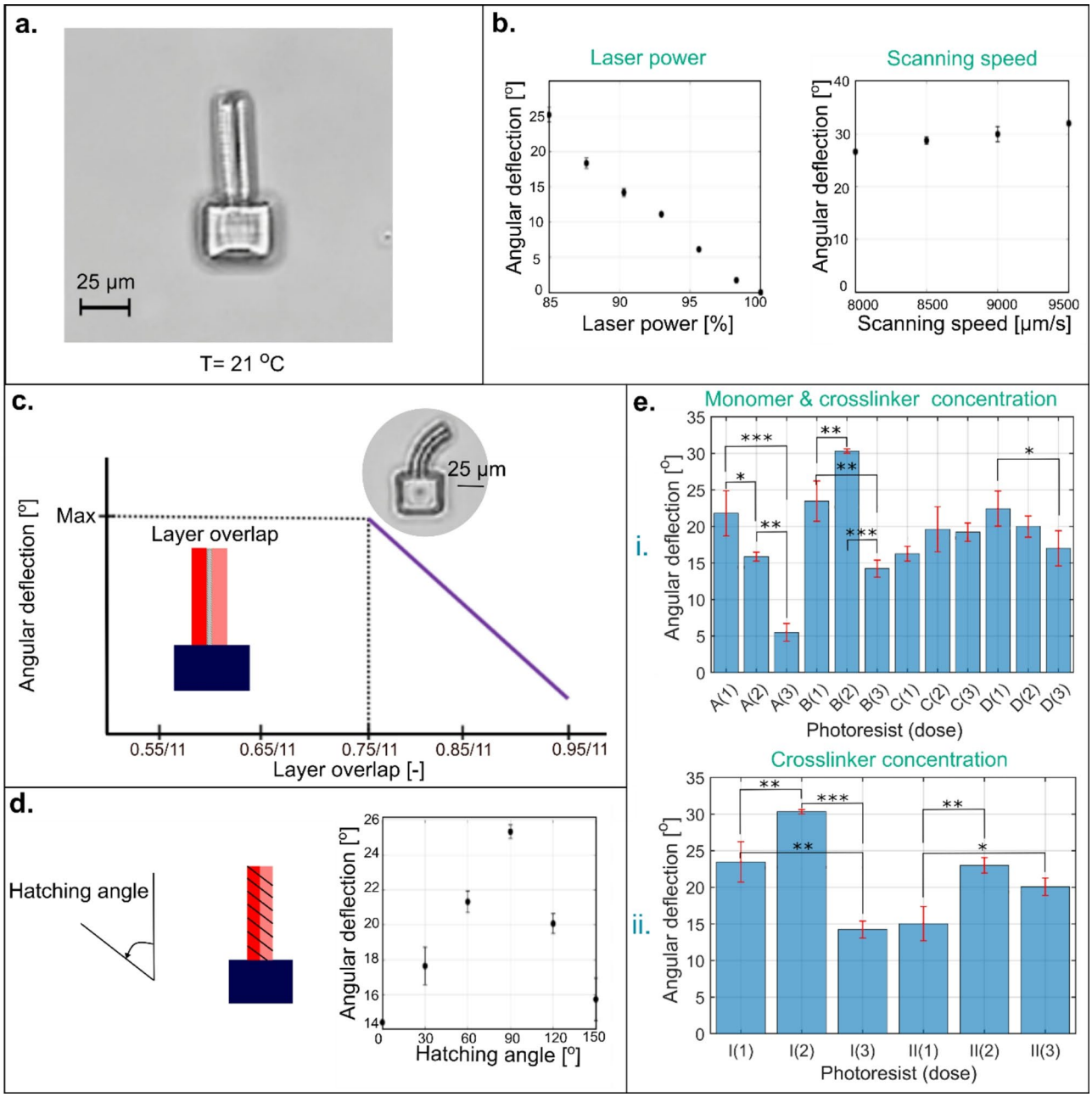

Fig. 2. **(a)** An optical image of the undeformed 4D-printed beam at a temperature of 21 °C, indicating the high quality of the print. **(b)** The effects of the laser power and scanning speed on the angular deflection of the bilayer beam (in degree). Note that the laser power of the laser source in terms of mW can be calculated as "laser power [mW] = 50×laser power [%]". **(c)** The effects of the overlap between the HLP and LLP layers on the angular deflection of the bilayer beam. **(d)** The assessment of the hatching angle on the angular deflection of the bilayer beam. **(e)** The effects of the chemical composition of the pNIPAM (i.e., monomer and crosslinker) on the angular deflection of the bilayer beams. A, B, C, D, and I and II represent various types of pNIPAM with different chemical composition concentrations. The numbers 1, 2, and 3 indicate a specific dose for each resin, reported in Tables 1 and 2. Statistical significance is denoted by *, **, *** corresponding to p-value < 0.05, p-value < 0.01, and p-value < 0.001, respectively. Bars without significance markers (e.g., *) indicate non-significance (p-value > 0.05). Moreover, note that DF_n and DF_d were respectively 2 and 6 for our ordinary ANOVA test corresponding to each set of experiments ($n = 3$).

density compared to laser power, resulting in smaller variations in thermal shrinkage between the HLP and LLP layers and, thus, less effect on shape morphing of 4D-printed microstructures. Consistent with prior studies[33], laser power more significantly affects the degree of polymerization and thermomechanical properties of 2PP printed microstructures, underscoring its dominant role in tuning shape-morphing behavior.

Effect of the overlap and hatching angle on angular Deflection of the bilayer beams

To further tune the shape-morphing behavior of bilayer beams, we investigated the effect of the overlap between the LLP and HLP layers, depicted as the gray region in Fig. 2c. Greater overlap is expected to increase beam rigidity, reducing angular deflection, but insufficient overlap risks delamination during post-chemical development process. To quantify this, we varied the normalized overlap (defined as the overlap distance divided by the total beam thickness 11 μm), from 0.55/11 to 0.95/11 and measured the resulting angular deflection (Fig. 2c). Normalization ensures generalizability within different length scales, as mentioned in the "Materials and methods". Overlaps below 0.75/11 led to delamination, while increasing the overlap from 0.75/11 to 0.95/11 significantly reduced deflection due to enhanced interlayer cohesion and stiffness. Consequently, we selected a normalized overlap of 0.75/11 as the optimal balance between structural stability and shape-morphing capability for this study.

Additionally, the printing pattern, specifically the hatching angle (the angle between the hatching lines and the *x*-axis), influences the thermomechanical properties of 2PP 3D printed microstructures, similar to other 3D printing techniques[3,34]. To optimize this parameter, we varied the hatching angle from 0° to 150° for both LLP and HLP layers and measured angular deflection (Fig. 2d). A hatching angle of 90° yielded the maximum deflection (25.5°), likely due to the alignment maximizing anisotropic thermal expansion differences between layers. Thus, all the specimens were 2PP 3D printed with 90° hatching angle. The effect of 3D printing pattern has also been studied in other studies, such as[22].

It should also be noted that the variation of the angular deflection vs. hatching angle exhibited near-symmetry around the hatching angle of 90°, reflecting the beams' symmetry (Fig. 2d). Slight asymmetries, with errors less than 6% (e.g., between hatching angles of 60° and 120°), could be from experimental imperfections, such as variations in the 2PP 3D printing process, crystals formation in the photoresist due to small temperature changes, optical imaging limitations, or inaccuracies in the angular deflection measurement. These errors, however, remain within typical experimental tolerances.

Effect of the chemical composition of the pNIPAM on the angular Deflection of the bilayer beams

The chemical composition of the pNIPAM-based photoresist, beyond 3D printing parameters, significantly influences the shape-morphing behavior of bilayer beams by tuning their stiffness, thermal expansion, and printability[35,36]. Notably, the crosslinking concentration (Mbis) alters the storage modulus (stiffness) and water release (shrinkage) during heating, directly impacting deflection[36]. To investigate this, we first kept the crosslinker-to-monomer molar ratio fixed at 0.073 and varied the concentrations of NIPAM and Mbis (photoresists A, B, C, and D in Table 1). We 3D printed bilayer beams using these photoresists and measured their angular deflection. To measure the angular deflection of the bilayer beams made from these photoresists, we performed a distinct set of dose tests on each photoresist to find the optimal laser power and scanning speed (as reported in Table 1). The angular deflection of photoresists A, B, C, and D (Fig. 2e-i) exhibited almost no consistent trend when the concentration of the Mbis and NIPAM increased. This lack of a clear trend may instead reflect differences in each photoresist's optimal printing conditions. Nevertheless, photoresist B achieved the highest deflection (30.33° at dose 2), with an average of 22.7° across three doses, among others. It should be noted that higher concentrations (concentration orders: photoresist A < B < C < D) increased viscosity and opacity, reducing printability and reproducibility due to possible crystallization. This is due to the constant concentration of the solvent (i.e., ethylene glycol) at 450 μL. Based on these results and the practical considerations in terms of reproducibility and resin homogeneity, photoresist B (Section "Materials and methods") was determined to exhibit the highest average angular deflection of 22.7° across the three sets of doses with a maximum angular deflection of 30.33° (dose 2, Fig. 2e).

Photoresist	Nipam [mg]	Mbis [mg]	Molar ratio [-]	Sample	High dose (laser power/scanning speed)	Low dose (laser power/scanning speed)
A	400	40	0.073	1	84%/4500	64%/11,500
				2	92%/5500	68%/8500
				3	100%/8000	85%/8000
B	450	45	0.073	1	88%/5500	64%/10,500
				2	84%/7500	72%/11,500
				3	100%/6500	64%/11,500
C	500	50	0.073	1	92%/7500	64%/11,500
				2	84%/5500	68%/10,500
				3	80%/4500	76%/11,500
D	600	60	0.073	1	92%/7500	64%/11,500
				2	88%/4500	64%/10,500
				3	100%/8500	68%/11,500

Table 1. The compositions of the pNIPAM hydrogels when the molar ratio was fixed at 0.073 (i.e., types A, B, C, and D). The corresponding laser power and scanning speed for the HLP and LLP of each photoresist have also been reported as samples 1, 2, and 3. Note that the laser power of the laser source in terms of mW can be calculated as "laser power [mW] = 50×laswer power [%]".

Next, we investigated the effect of varying the crosslinking concentration (or the crosslinking-to-monomer molar ratio) while maintaining NIPAM at a constant concentration of 450 mg (Table 2, photoresists I–IV). Similar to the previous test, we performed distinct dose tests for each photoresist to find their optimal printing dose. The results of the photoresists I, II, III, and IV (Section "Materials and methods") indicated that increased crosslinking concentration likely decreases the angular deflection of the bilayer beams (Fig. 2e-ii). This is due to the effect of the crosslinking concentration on the degree of crosslinking, which in turn affects the water release during heating and the stiffness of the hydrogel. While a lower molar ratio enhances swelling, especially at low temperatures[37], practical considerations, including printing suitability and mechanical stability of our bilayer beams, limit further reduction in crosslinking concentration. The photoresists III and IV, with reduced crosslinking levels, therefore, lacked sufficient mechanical stability, resulting in bilayer beam collapse. We selected photoresist I, which has the highest average angular deflection of 22.7°, as reported in Table 2. Note that the photoresist I (2) or B(2), as the optimal photoresist with a molar ratio of 0.0734, 450 mg of NIPAM, and 45 mg of Mbis, was chosen for 3D printing all other specimens. The optimal dose for this photoresist was 84% laser power, with a speed of 7500 µm/s for the HLP layer and 72% laser power, at a speed of 11,500 µm/s for the LLP layer.

Effect of temperature on the angular Deflection of the bilayer beams and their FEM validation

The angular deflection of the beams is also dependent on the temperature in such it increases with temperature (Fig. 3a). However, above a threshold of approximately 60 °C, the angular deflection stabilizes, reaching a plateau at around 30° (Fig. 3a), indicating a threshold point in the bilayer beam's shape-morphing capability. Such relatively low actuation range (i.e., ~ 32 °C to 60 °C) makes pNIPAM a favourable smart material, among others, such as PLA with a relatively high working temperature[3]. At 37 °C, a temperature relevant to applications requiring compatibility with physiological conditions, the bilayer beams exhibited partial shape morphing, with an angular deflection of approximately 18° (Fig. 3a-i and ii).

According to the experimental results of the temperature-dependent angular deflection, we also validated our FEM predictions (Fig. 3a-i and Section "Materials and methods"). At temperatures of 21 °C and 30 °C, the FEM results closely aligned with experimental measurements, demonstrating the model's accuracy at lower temperatures. However, at 40 °C, a noticeable discrepancy was observed between the experimental data and the FEM predictions. This mismatch can be attributed to several factors: *(i) Measurement errors*: inaccuracies in determining the thermal expansion coefficients for the LLP and HLP layers, derived from the linear slope of the plot in Fig. 3b-iv, may contribute to the error. Note that the data exhibit some nonlinearity, challenging the assumption of a constant coefficient. *(ii) Environmental variability*: fluctuations in ambient temperature and humidity during experiments could affect the beam's response. (iii) 3D printing imperfections: The 3D printing may introduce structural inconsistencies that deviate from the idealized FEM geometry. *(iv) Model assumptions*: The FEM assumes temperature-independent elastic modulus and thermal expansion coefficients, which may not fully capture the material's behavior at higher temperatures. *(v) Temperature control*: Experimental errors in maintaining precise temperature conditions could further cause discrepancies.

Measurement of the thermal expansion coefficients of the pNIPAM beams

We measured the thermal expansion coefficients of the pNIPAM beams along thier length (longitudinal expansion ratio), width (transverse expansion ratio), and thickness (depth expansion ratio) (Fig. 3b) for both HLP (i.e., a laser power of 84% and a scanning speed of 7500 µm/s) and LLP (i.e., a laser power of 72% and a scanning speed of 11500 µm/s) doses, as depicted in Fig. 3b. The LLP beams consistently exhibited a higher thermal expansion coefficient across all the directions (Fig. 3b-i, ii, and iii), a result attributed to their lower degree of

Photoresist	Nipam [mg]	Mbis [mg]	Molar ratio [-]	Sample	High dose (laser power/scanning speed)	Low dose (laser power/scanning speed)
I	450	45.00	0.073	1	88%/5500	64%/10,500
				2	84%/7500	72%/11,500
				3	100%/6500	64%/11,500
II	450	30.70	0.05	1	88%/5500	68%/11,500
				2	80%/5500	64%/10,500
				3	88%/7500	64%/11,500
III	450	12.30	0.02	1	96%/7500	76%/8500
				2	88%/6500	80%/10,500
				3	84%/5500	76%/9500
IV	450	6.15	0.01	1	NA	NA
				2	NA	NA
				3	NA	NA

Table 2. The compositions of the pNIPAM hydrogels when the NIPAM concentration was fixed at 450 g (i.e., types I, II, III, and IV). The corresponding laser power and scanning speed for the HLP and LLP of each photoresist have also been reported as samples 1, 2, and 3. Note that the laser power of the laser source in terms of mW can be calculated as "laser power [mW] = 50×laswer power [%]".

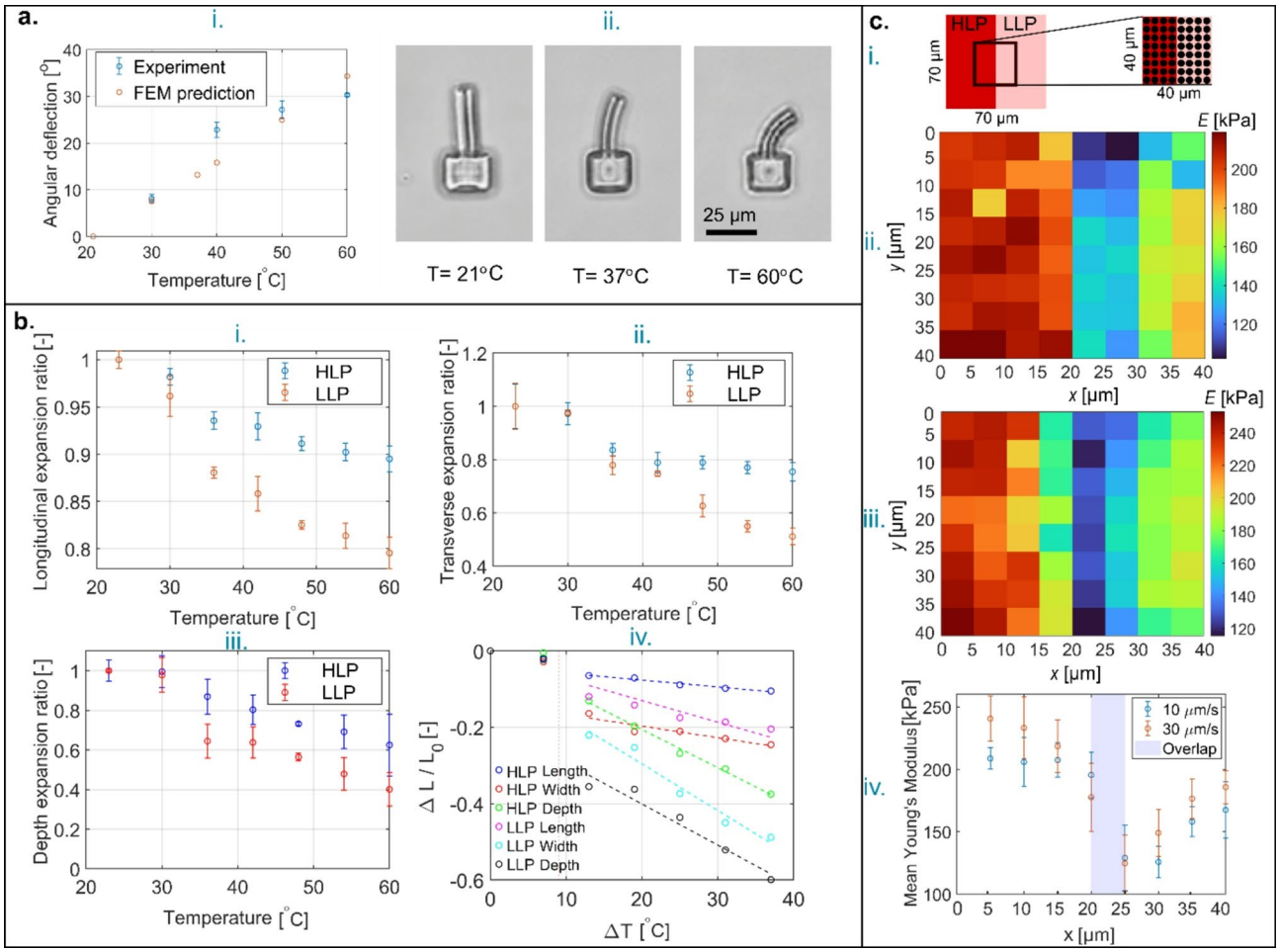

Fig. 3. Thermomechanical characterization of pNIPAM. **(a)** The effects of temperature on the angular deflection of the bilayer beam within 21 °C and 60 °C, experimentally and numerically (**i**). The optical images show the deflection of the deformed bilayer beam at different temperatures of 21 °C, 37 °C, and 60 °C (**ii**). **(b)** Thermal expansion coefficients (longitudinal, **i**, transverse, **ii**, depth, **iii**) of the HLP and LLP beam as a function of temperature. The variation of the expansion ratio across different directions for each HLP and LLP (**iv**). **(c)** The Young's modulus measurement of pNIPAM at 21 °C and at two different loading rates. The schematic drawing shows the configuration for measuring the Young's modulus of pNIPAM with LLP, HLP, and at the interface between the doses (**i**). The heatmap shows the Young's modulus of pNIPAM at a low loading rate of 10 μm/s (**ii**). The heatmap represents the Young's modulus distribution within pNIPAM at a high loading rate of 30 μm/s. The spatial variation of the Young's modulus of pNIPAM 3D printed with LLP, HLP, and at the interface at different loading rates.

polymerization, which increases their sensitivity to temperature changes. The thermal expansion coefficients across all the directions were lower for lower temperatures (e.g., 30 °C) than those at higher temperatures (e.g., 60 °C). Moreover, as temperature increased beyond 30 °C, the disparity in thermal expansion coefficients between the HLP and LLP layers became more highlighted, especially along the longitudinal direction, while the depth direction showed minimal variation. Additionally, a plateau was observed ~ 60 °C, beyond which further temperature increases did not alter the expansion coefficients.

To quantify these trends, we plotted the relative dimensional change (change in dimension divided by initial dimension) vs. temperature (Fig. 3b-iv) and calculated the thermal expansion coefficients (in 1/°C) from the slopes. The results, summarized in Table 3, highlight anisotropic thermal expansion, with the magnitude varying significantly depending on the measurement direction. This anisotropy likely occurs from the combined effects of printing direction and hatching angle, which influences crosslinking density in a direction-dependent manner.

Measurement of the young's modulus of the pNIPAM hydrogel

The average Young's modulus of the 2PP 3D-printed pNIPAM blocks at different laser doses (i.e., LLP and HLP), and specifically their interface, ranged from 120 kPa to 240 kPa at a temperature of 21 °C (Fig. 3c). As expected, the LLP layer exhibited a lower Young's modulus for both loading rates (150.3 kPa on average for the low rate (i.e., 10 μm/s) and 170.4 kPa for the high rate (i.e., 30 μm/s)). In contrast, the HLP region exhibited higher

Direction	HLP [1/° C]	LLP [1/° C]
x	−0.0018	−0.0057
y	−0.01	0.0107
z	−0.0030	−0.0122

Table 3. The thermal expansion coefficients of the pNIPAM hydrogel across three orthogonal directions for the HLP and LLP doses.

Young's modulus due to higher degree of crosslinking (207.3 kPa for the low rate and 230.8 kPa for the high rate) (Fig. 3c-ii, iii, and iv).

The difference in the Young's modulus corresponding to different loading rates reflects the viscoelastic nature of the pNIPAM hydrogel. Considering the time-dependency of the hydrogel, it is stiffer at a higher loading rate (i.e., 30 µm/s) as its molecular chains have less time to rearrange under mechanical stress[38]. On the other hand, at lower rates, the network can relax and redistribute internal stresses, resulting in a lower apparent modulus.

The spatial distribution of the average Young's modulus at the low loading rate (Fig. 3c-ii) is more homogeneous in the HLP layer compared to the high loading rate. This variation is likely attributed to local imperfections or surface roughness introduced during high-dose 3D printing, which can introduce errors in nanoindentation, especially given the small indentation depth (~ 1 µm). Similar effects were also observed in the LLP region at both loading rates.

Interestingly, the interface region (x = [20 25] µm in Fig. 3c-iv) showed the lowest Young's modulus (125–190 kPa at both loading rates). Although repeated exposure is generally expected to increase crosslinking and thus Young's modulus, the reduced modulus at the interface is likely influenced by fabrication-induced imperfections (or surface roughness), such as poor interlayer adhesion or the formation of micropores due to localized overpolymerization. This could be due to the fabrication process, as the HLP layer is first 3D printed, followed by the LLP layer.

These interfacial effects may affect the reliability of nanoindentation measurements, particularly in thin, layered geometries where surface continuity plays a critical role. To better understand the mechanical behavior at the interface, further validation is recommended, such as using alternative techniques (e.g., atomic force microscopy-based nanoindentation) or high-resolution microscopy (e.g., confocal microscopy) to characterize material homogeneity and structural integrity at the interface.

It should be noted that the indentation curves of the pNIPAM hydrogel (Figure S1, supplementary document) exhibit a fully nonlinear elastic response, which is typical for hydrogels. Capturing such non-linear behavior, particularly at larger deformations, generally requires the use of hyperelastic models, such as Mooney-Rivlin or Ogden formulations[39]. A challenge in using more advanced hyperelastic models is the fact that multiple material parameters make it difficult to compare the properties of different materials easily. Given that the goal of this study was not to fully characterize the constitutive behavior of the hydrogel, but rather to compare the Young's modulus across different fabrication conditions, we approximated the mechanical response as linearly elastic, using Young's modulus as a comparative metric.

It is important to note that the measured Young's modulus may vary, depending on the applied strain. For example, based on the indentation data shown in Figure S1 of the supplementary document, the Young's modulus calculated at lower indentation depths (below 500 nm) is smaller than that at higher depths (500–1000 nm), reflecting the strain-dependent stiffening behavior of the hydrogel. To maintain consistency throughout the study, we extracted the modulus from the loading segment of the indentation curve using the Hertzian model, as is commonly used in similar studies[40]. Additionally, slight variations in the unloading stage were observed, likely due to adhesion effects at the tip-sample interface, as also observed in the representative curves in Figure S1 of the supplementary document.

Shape recovery of the pNIPAM bilayer beams after dehydration

The performance of the dehydrated pNIPAM bilayer beams was also assessed. Upon drying, the hydrogel structures lost water and shrank significantly (Supplementary Video S2). Once rehydrated by immersion in water, the microstructures returned to their original geometries (Supplementary Video S3), indicating the robustness and structural integrity of the bilayer design at the microscale.

In addition, the pNIPAM hydrogel beams exhibited reversible shape morphing in response to temperature changes, demonstrating their ability to actuate over multiple cycles. Previous studies have reported the successful use of 2PP-fabricated pNIPAM structures for at least 20 actuation cycles without significant degradation[4,41]. However, in the present study, we did not quantify the number of cycles or changes in the deflection across repeated actuations. Further investigation is required to assess the long-term durability and fatigue behavior of the bilayer beams under repeated thermal cycling.

Potential shape-morphing applications of 2PP 4D-printed microstructures

To demonstrate the versatility of 2PP 4D printing with pNIPAM, we investigated a range of shape-morphing behaviors in bilayer beams by varying both layer arrangement and 3D printing parameters. The undeformed configuration of the microstructures at 21 °C and their deformed states in water at 60 °C are depicted in Fig. 4, along with their corresponding von Mises stress contours (in MPa) predicted by our FEM. All microstructures were 3D printed at a consistent height (Z) on a single post, and their activation time was less than 1 s, faster than many comparable temperature-responsive 4D-printed systems, such as FDM 4D printing of polylactic acid

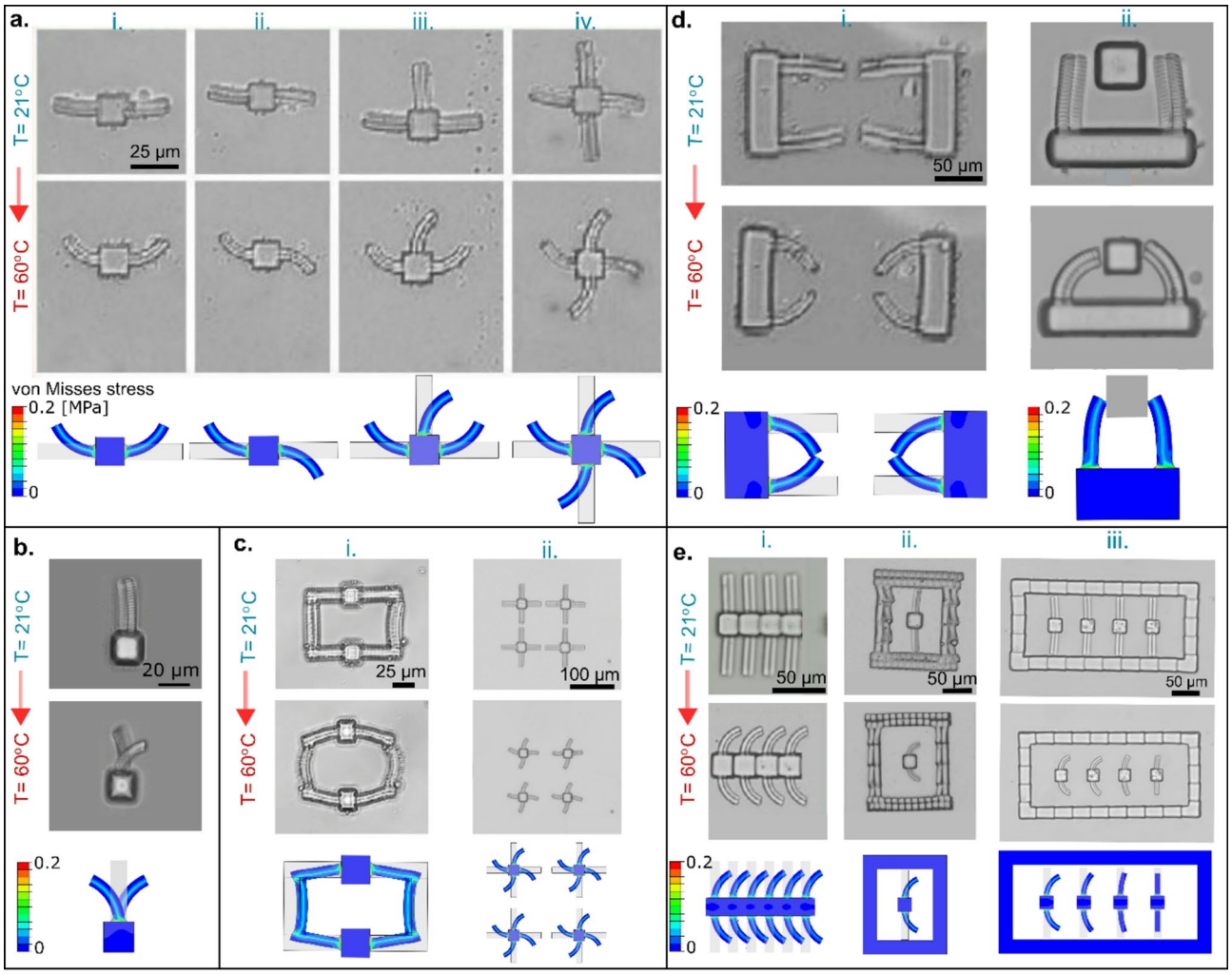

Fig. 4. Optical images of shape-morphing behavior in proof-of-concept applications of 2PP 4D-printed microstructures with their corresponding FEM prediction. Note that the contour indicated the distribution of von Mises stress in terms of MPa. **(a)** The in-plane bending deformation of bilayer beams (**i**), twisting/shrinkage deformation (**ii**), three-beam bending/twisting deformation (**iii**), and fully twisting deformation (**iv**). **(b)** The out-of-plane bending deformation at different heights (Z). **(c)** A unit cell of a metamaterial featuring a switchable Poisson's ratio when temperature changes (**i**). A unit cell block representing a metamaterial with a negative Poisson's ratio (or auxeticity) when temperature increased by 60 °C (**ii**). **(d)** A simple grasping mechanism (**i**), and a proof-of-concept application of a soft gripper, in which it holds an object (**ii**). **(e)** A proof-of-concept microfluidic system of the 2PP 4D printing with shape-morphing capability. A series-bending mechanism that can open up a membrane as a valve simultaneously or sequentially (**i**), and a microfluidic mechanism in which increasing the temperature leads to potential flow (**ii**). A 4D-printed proof-of-concept microfluidic system in which the beams are activated gradually from the maximum (left beam) deflection to the minimum (right beam) when temperature increases by 60 °C (**iii**).

(PLA)[24]. This section highlights applications in soft robotics and microfluidics, enabled by systematic parameter tuning and predictive modeling.

Simple in-plane shape morphing was achieved through varied bilayer beam configurations, each using differences in HLP and LLP layer arrangements to induce distinct deformations, as shown in Fig. 4a. Such basic shape morphing in bilayer beams is one of the common examples of the versatility of 3D printing smart materials at the microscale[2,4,26,28,42–47]. A single beam with uniformly ordered HLP and LLP layers produces simple bending, ideal for soft robotic actuators or touch-sensitive sensors under cyclic loading, and adaptable as a gripper for microscale objects if extended in length (Fig. 4a-i). Inverting the HLP and LLP order induces coupled in-plane twisting and shrinkage, enabling applications, such as helical microactuators for soft robotics (Fig. 4a-ii). Adding a second beam to this twisting configuration enhances in-plane deformation complexity, demonstrating scalability for multi-beam systems (Fig. 4a-iii). A four-beam arrangement, connected only at a single post, achieves isotropic twisting and shrinkage, potentially functioning as a unit cell for programmable metamaterials[48,49] with potential in soft robotics or adaptive structures (Fig. 4a-iv). In all cases, beams remain unattached except at the post to avoid boundary constraints, though slight post deformation introduces minor

deviations from desired beam deflections despite high-dose 3D printing. The FEM accurately predicts these deformations, with higher von Mises stress at the HLP/LLP interface due to overlap, aligning closely with experimental observations (Fig. 4a).

The out-of-plane deformation was also achievable by 4D printing two beams at different heights, *Z*, ideal for soft robotics applications needing multi-directional motion (Fig. 4b). The FEM accurately predicts deformation, with stress distributions similar to in-plane cases, underscoring the model's versatility.

By combining in-plane deformations with geometric constraints, we demonstrated a temperature-responsive unit cell for programmable metamaterials, designed to exhibit tunable mechanical properties such as Poisson's ratio (i.e., the negative ratio of lateral strain to longitudinal strain) (Fig. 4c). Note that in non-stochastic metamaterials[48], a unit cell refers to a repetitive geometric pattern that represents the overall properties of the material, with the entire meta-biomaterial composed of an array of such unit cells[48]. We aimed at 4D printing unit cell whose Poisson's ratio changes over time by changing temperature. However, it is noted that the difficulty level increases when the number of unit cells increases, mainly due to the geometrical constraints, which depend on the stiffness of the struts.

In one configuration, a unit cell with two bilayer beams as vertical struts and two high-dose single-layer beams as horizontal struts transitions from a rectangular shape (near-zero Poisson's ratio[50]) at 21 °C to a honeycomb-like structure (positive Poisson's ratio[50]) at 60 °C, as shown in Fig. 4c-i and Supplementary Video S4. However, unintended deformation of the supporting post, despite its high-dose printing, caused minor deviations in the horizontal struts, affecting the desired shape morphing. The FEM predictions for this unit cell showed slight discrepancies, likely due to the assumption of a non-deformable post.

In another design, four bilayer beams arranged in a twisting-shrinkage configuration formed a unit cell that contracts uniformly at 60 °C, exhibiting auxetic behavior (negative Poisson's ratio, Fig. 4c-ii). This auxetic response, suitable for adaptive structures in soft robotics, was accurately captured by the FEM, with close agreement between experimental and predicted deformations. Scaling these unit cells into larger arrays poses challenges due to increased geometric constraints and strut stiffness, highlighting the need for further optimization to achieve complex 3D metamaterials.

We further demonstrated proof-of-concept microstructures for potential soft robotic applications (Fig. 4d-e). We 4D printed a two-beam structure on a large post as a grasping mechanism which is activated by temperature increases (to maximum of 60 °C), making it suitable for delicate microscale manipulation (Fig. 4d-i). The FEM predictions align closely with observed deflections, with minor discrepancies attributed to variations in thermal expansion coefficients and printing imperfections. To quantify actuation, we designed a system with an additional post printed at the same high dose, where a beam deforms at 60 °C until contacting the post, yielding a maximum FEM-predicted force of approximately 0.085 μN, ideal for micro-actuating, such as atomic force microscopy of cells[51] (Fig. 4d-ii).

We also proposed a proof-of-concept application for microfluidic systems comprising a chamber and valves made of bilayer beams that function as temperature-responsive valves, which can regulate fluid flow by controlling the opening and closing of the valve (Fig. 4e). The current proof-of-concept microfluidic system could be upgraded by incorporating the 4D printing of multiple beams or posts with controlled deformation (Fig. 4e-i). Extending this concept, a gradient flow control system was achieved by 3D printing four bilayer beams with a consistent LLP layer (72% laser power, 11500 μm/s scanning speed) and HLP layers varying progressively (decreasing laser power by 4% and scanning speed by 1334 μm/s per beam, Fig. 4e-iii). This configuration enables remote valve opening, enhancing precision in microfluidic applications. The FEM accurately predicts bilayer beam deflections across these designs, validating the model's reliability for optimizing shape morphing in 2PP 4D-printed microstructures.

Conclusions

In conclusion, we utilized a single-material, and a single-step fabrication process based on 2PP direct laser writing and pNIPAM-based photoresist to fabricate smart 3D microstructures capable of reversible and rapid shape morphing upon temperature change. Through a systematic study, we investigated the effects of printing parameters (e.g., laser power, scanning speed and hatching angle) and photoresist compositions (NIPAM and Mbis) on the angular deflection of the bilayer beams, considering the mechanical stability and printability of the bilayer beams.

To predict the thermomechanical behavior of the 2PP 4D-printed microarchitectures, we employed a straightforward computational model based on the experimental characterization of the pNIPAM. This included measuring the thermal expansion coefficients over a range of temperatures and the Young's modulus under two different loading rates. The validated computational model enabled us to rationally design proof-of-concept demonstrations for soft robotics and microfluidic systems, such as soft grippers and temperature-responsive valves. Shape morphing in these applications was achieved by introducing thermomechanical anisotropy through localized variations in crosslinking degree, which were achieved by changing 3D printing parameters.

Our results highlight the critical role of both photoresist composition and printing parameters in tailoring the performance of 4D-printed microstructures, in terms of shape morphing, mechanical stability, and printability. This work advances the field of smart 3D microstructures, particularly for soft robotics and microfluidic systems, by experimentally characterizing the thermomechanical properties of the pNIPAM and providing a predictive computational model. While these findings lay the groundwork for potential future applications in other areas, such as biomedical devices, additional studies are needed to validate their feasibility and functionality in such contexts.

Materials and methods

Photoresist composition and Preparation

NIPAM (see weights in Tables 1 and 2) was added to 450 µL of ethylene glycol (EG) and magnetically stirred for 3 h. After complete dissolution, the cross-linker N, N-methylenebis(acrylamide) (Mbis) (Tables 1 and 2) and 15 mg (1.49%w/w) of the photo-initiator lithium phenyl(2,4,6-trimethylbenzoyl)phosphinate (LAP) were added under yellow light conditions and magnetically stirred again for 3 h. Following this, the brown bottle containing the photoresist solution was wrapped in an aluminum foil to avoid unnecessary exposure to light. The photoresist was stored for short periods (on a weekly basis) in a cleanroom environment with controlled temperature and humidity maintained at 19.9 °C ± 1.2 °C and 53.5% ± 10.25%, respectively. To maintain homogeneity and ensure printability, the photoresist was magnetically stirred for 20 min before each use. It should also be noted that the recipe of the pNIPAM composition and preparation process were adapted from Hippler et al.[4].

As the photoresist's chemical composition significantly affects the bilayer beams' angular deflection, we varied the ratios of the NIPAM and Mbis. Consequently, we developed eight different types of photoresists (i.e., A, B, C, D, I, II, III, and IV) (Tables 1 and 2). In photoresists A, B, C, and D, the molar ratio of the crosslinking to monomer was fixed at 0.073, and the ratios of the monomer and the crosslinking were varied accordingly. On the other hand, in photoresists I, II, III, and IV, the ratio of NIPAM was fixed at 450 mg, but the Mbis ratio was varied. It should be noted that the notations "1", "2", and "3" indicate the different doses (laser power and scanning speed) for each photoresist. This is because we performed a new dose test for each photoresist and selected different doses to measure the angular deflection of the bilayer beams. We 3D printed the bilayer beams with the same printing setting, and the printing parameters were chosen based on the corresponding dose test (Tables 1 and 2).

Fabrication and post-processing of the microarchitectures

All structures in this study were fabricated using a commercial direct laser writing setup (Photonic Professional GT+, Nanoscribe GmbH) (Fig. 1c). The initial designs (i.e., beams) were generated using SolidWorks (Dassault Systèmes, France), a commercial computer-aided design (CAD) software, and then exported as.stl files. These files were imported into DeScribe software (Nanoscribe, Germany) to generate General Writing Language (.gwl) files, which were subsequently utilized in the Nanowrite software (printing software, Nanoscribe, Germany) to interface with the 2PP 3D printer, enabling the fabrication process. The printing was executed using a Photonic Professional GT + 3D printer (Nanoscribe). The setup utilizes a femtosecond fiber laser operating at a wavelength of 780 nm, with a typical maximum output power of 50 mW (equivalent to 100% power), a repetition rate of 80 MHz, and a pulse duration of 100 femtoseconds.

The conventional direction of printing in DeScribe (software for print job preparation from Nanoscribe) is along the X-Y plane (i.e., individual layers are printed along the X-Y plane), and the layers are stacked upon each other along the Z-axis to obtain the desired structure. However, due to the low scanning speed of 3D printing (8,000 µm/s), delamination was observed between two consecutive layers along the Z-axis. Therefore, the printing strategy was modified to include small sections of 2 µm in length, which were 3D printed along the X-axis (corresponding to the length of the beam) (Fig. 1d), with slicing and hatching distances of 0.3 and 0.2 µm, respectively. To identify the maximum thickness of the slices along the X direction, we conducted a parametric study and concluded that 2 µm is the desirable size. It should also be noted that the shape morphing and the stability of the beams were dependent on the 3D printing sequence of the HLP and LLP layers. Here, we initially started printing from the HLP layer. An overlap of 0.75 µm (equivalent normalized overlap of 0.75/11) was provided between the HLP and LLP layers to prevent delamination in the structure when subjected to thermal loads. Additionally, an overlap of 2 µm was chosen between the beam element and the fixed post to ensure the structural stability of the overhanging structure. Moreover, we employed the piezo scanning mode instead of the z-drive for the stage movement due to the small dimensions of our specimens and to increase the stability of the photoresists. It should also be noted that in the oil configuration, we are limited to the working distance of the employed 25×, which is 380 µm. Considering the thickness of the coverslip substrates, which is 170 µm, microstructures up to a maximum height of ~ 210 µm can be 3D printed.

Prior to printing the microstructures, a rounded glass substrate with a diameter of 30 mm and a thickness of 170 µm (Thermo Scientific Inc., USA) was first cleaned using isopropanol and acetone (both from Sigma-Aldrich, Germany). This was followed by oxygen plasma treatment (Diener electronic GmbH, Germany) of the glass substrate at a power of 80 W, with a gas flow rate of 5 cm^3/min and a pressure of 0.12 bar, for 15 min. The treated glass substrate was then placed in a petri dish containing a thin layer of 3-(Trimethoxysilyl)propyl methacrylate (stabilized with BHT, 98.0%, Sigma-Aldrich, Germany) for 1 h. This process, commonly referred to as silanization, ensures that the microstructures printed on the glass substrate adhere firmly to it, thereby reducing the likelihood of delamination of the structures. Following silanization, the glass substrate was again cleaned using isopropanol. The glass substrate was then firmly mounted onto the substrate holder with adhesive tape. Since the oil configuration was used for fabricating the structures, a drop of immersion oil (Immersol 518 F, Carl Zeiss, Oberkochen, Germany) was placed on the side of the substrate facing the objective.

Next, a drop of the pNIPAM-based photoresist was placed on the other side of the glass substrate, and the sample holder was loaded into the printer. A 25× oil immersion objective (numerical aperture of 0.8; Carl Zeiss, Oberkochen, Germany) was used for printing the microstructures. Once the printing process was completed, the excess precursor solution was rinsed away using acetone, followed by rinsing with ultrapure water.

Post-processing of the 3D-printed microstructures included dipping the substrate into acetone for 30 s, followed by 10 min of upright immersion in a glass container filled with demineralized-water. Afterward, the substrate was attached to a petri dish using two drops of silicone glue, and the substrate was covered with demineralized-water for 5 min, ensuring the silicone glue was not wetted, to allow it to dry. Finally, the rest of the petri dish was filled with demineralized-water (approximately 5 mm deep) and left at room temperature

for 2–3 h to allow the hydrogel structures to rehydrate before any tests were performed. This duration (i.e., 2–3 h) was obtained by conducting a study on the effect of the dehydration duration on the angular deflection in a laboratory environment with an average temperature and humidity of 19.9 °C and 53.5%, respectively.

Beam deflection

To find the optimal printing parameters and material compositions, and to quantify our developed hydrogel, we first performed experiments on a beam with a size of $40 \times 11 \times 12$ μm^3, alongside x, y, and z (Fig. 1b and d). Each beam was joined at one end to a $20 \times 20 \times 25$ μm^3 base (the blue block in Fig. 1b), which is adhered to the glass substrate. The beam's deflection level was indicated via the angular deflection, as illustrated in Fig. 1b. The angular deflection of the beam is defined as the angle between the midpoint at the end of the bilayer beam and the line orthogonal to the interface's face between the support structure and the bilayer (Fig. 1b). It should be noted that the thermomechanical characterization of the 2PP 4D-printed microarchitectures were measured in a chemistry laboratory with controlled temperature and humidity around 22 °C ± 3 °C and 60% ± 10%, respectively.

After finding the optimal dose (laser power and scanning speed) from a dose test (Figure S1 of the supplementary document), we printed three beams (with the post) for each application and assessment. It should be noted that the beams had a pre-deflection in some cases due to the pNIPAM's development process. Nevertheless, this pre-deflection vanished after reheating them, releasing the residual stress.

Thermomechanical characterization of pNIPAM

Mechanical characterization of the specimens involved determining the thermal expansion coefficients of the beams, as well as performing nanoindentation to assess the Young's modulus of the pNIPAM at various loading rates. Three beams ($n = 3$) were 3D printed with the same dimensions as before to determine how the beam shrinks at various temperatures. However, only one dose throughout was used (i.e., either HLP or LLP). The angular deflection vs. temperature was recorded. Moreover, the thermal expansion ratios were determined by submerging the specimens in a water bath at different temperatures and then comparing the longitudinal, depth, and transverse dimensions before and after exposure to hot water.

Nanoindentation was used to determine the Young's modulus of the pNIPAM. This is a process whereby the mechanical properties of the specimens are characterized using an optical interferometry-based nanoindenter (Chiaro, Optics11 life, The Netherlands). During the application of the load, the displacement of the cantilever, equipped with a spherical glass probe, is recorded, resulting in a force-displacement curve from which the sample's mechanical properties can be determined. The nanoindenter employed in this work had a 2.5 μm radius probe with a nominal stiffness of 0.43 N/m. All nanoindentations were performed with the sample submerged in demi-water. Cuboids measuring $70 \times 70 \times 20$ μm^3 were printed using the doses described above and left for 20 h before nanoindentation to ensure the samples had reached a swelling equilibrium and to ensure repeatability in the measurements. The Young's modulus of each specimen was calculated using the Hertzian model, assuming linear elastic behavior in the pNIPAM hydrogel. This model is typically applied to soft materials[40], such as pNIPAM in this work. The loading regime used was a peak indentation waveform with a controlled maximum load of 0.4 N (corresponding to approximately 1 μm indentation depth. Two different loading rates were used, initially a loading rate of 10 μm/s, followed by a loading rate of 30 μm/s. Following the HLP and LLP layers interface, a 4.75 μm overlap (maintaining the same overlap-to-width ratio as in the bilayer beams) was selected. It should also be noted that we first printed the HLP layer followed by the LLP layer.

Computational modeling

We used the commercial software suite Abaqus/CAE 2023.HF2 (Dassault Systèmes Simulia Corp., Johnston, RI, USA) for finite element analysis. The analysis incorporated nonlinear geometric effects to capture the large deflections observed in the bilayer beams. Linear thermally-coupled brick elements with full integration (C3D8T, Abaqus) were utilized to model the behavior of the bilayer microarchitectures. A systematic mesh convergence study was performed to find the optimal mesh size by changing the mesh size from 3 μm to 0.5 μm. The angular deflection did not change anymore within a tolerance of 5% by considering a mesh size of 1 μm, and therefore, we chose this mesh size for modeling the microarchitectures. A uniform temperature, ranging from ambient temperature (20 °C) to 60 °C, was applied to conduct a coupled temperature-displacement steady-state analysis. The material model included Young's moduli (i.e., E) and orthotropic thermal expansion coefficients to replicate the anisotropic behavior observed in experiments. These material properties were derived from experimental data (Figs. 3c; Table 3).

For the analysis of bilayer deflection, the angular displacement between the beam tip at the interface of HLP and LLP layers was quantified relative to the initial interface line (Fig. 1b). The beam substrates were modeled as fixed, with a relatively high Young's modulus (e.g., $E = 100$ MPa) assigned to ensure the base rigidity. Standard surface-to-surface contact was defined for simulations involving a gripper and object, with hard contact in the normal direction and friction modeled using a penalty coefficient of 0.2. The object was represented as an analytical rigid part, further simplifying the interaction modeling.

Statistical analysis

We used Prism (9.4.1, GraphPad, USA) software for the statistical analysis (i.e., mean values, standard deviations and the p-values) of the effect of the chemical compositions of the pNIPAM on the angular deflection of the bilayer beams. All the experiments were repeated three times ($n = 3$). Prior to calculating the p-value, we first performed a normality test using the Shapiro-Wilk test with alpha= 0.05 to determine the normality of the data. After ensuring the normality of data in each group (at each dose), we performed an ordinary one-way ANOVA test, followed by *post-hoc* analysis using Tukey's multiple comparison test to calculate the p-value between

groups. We considered a p-value< 0.005 as statistically significant for all the experiments. It should also be noted that the DF_n and DF_d presented in the caption of Fig. 2 indicate the degree of freedom for the numerator of the F ratio and the denominator, respectively.

Data availability

The data that support the findings of this study are available from the corresponding author [M. J. M] upon reasonable request.

Received: 3 February 2025; Accepted: 6 June 2025
Published online: 01 July 2025

References

1. Yarali, E. et al. 4D Printing for Biomedical Applications. *Advanced Materials* **36**, 2402301 (2024). https://doi.org/10.1002/adma.202402301https://
2. Tan, L., Yang, Y., Fang, L. & Cappelleri, D. J. Shape-Programmable Adaptive Multi-Material Microswimmers for Biomedical Applications. *Advanced Functional Materials* **34**, 2401876 (2024). https://doi.org/10.1002/adfm.202401876
3. Moosabeiki, V. et al. Curvature tuning through defect-based 4D printing. *Commun. Mater.* **5** (1), 10 (2024).
4. Hippler, M. et al. Controlling the shape of 3D microstructures by temperature and light. *Nat. Commun.* **10** (1), 1–8 (2019).
5. Peng, S. et al. Magnetic-Driven Micro-Gear pair fabricated by femtosecond laser writing. *Adv. Eng. Mater.* **26** (10), 2301960 (2024).
6. Yarali, E., Zadpoor, A. A., Staufer, U., Accardo, A. & Mirzaali, M. J. Auxeticity as a Mechanobiological tool to create meta-biomaterials. *ACS Appl. Bio Mater.* **6** (7), 2562–2575 (2023).
7. Wang, W. et al. Two-photon polymerization-based 3D micro-scaffolds toward biomedical devices. *Chemical Engineering Journal* **493**, 152469 (2024). https://doi.org/10.1016/j.cej.2024.152469
8. Li, H. et al. Reconfigurable 4D printing via mechanically robust covalent adaptable network shape memory polymer. *Sci. Adv.* **10** (20), eadl4387 (2024).
9. van Manen, T., Dehabadi, V. M., Saldívar, M. C., Mirzaali, M. J. & Zadpoor, A. A. Theoretical stiffness limits of 4D printed self-folding metamaterials. *Commun. Mater.* **3** (1), 43 (2022).
10. Zeng, J. et al. Additive manufacturing of high entropy shape memory alloy with outstanding properties through multi-remelting in-situ alloying. *Additive Manufacturing* **88**, 104253 (2024). https://doi.org/10.1016/j.addma.2024.104253
11. Wang, R. et al. Direct 4D printing of ceramics driven by hydrogel dehydration. *Nat. Commun.* **15** (1), 758 (2024).
12. Wan, L. et al. Direct 4D printing of gradient structure of ceramics. *Chem. Eng. J.* **465**, 142804 (2023).
13. Sartori, P., Yadav, R. S., del Barrio, J., DeSimone, A. & Sánchez-Somolinos, C. Photochemically Induced Propulsion of a 4D Printed Liquid Crystal Elastomer Biomimetic Swimmer. *Advanced Science* **11**, 2308561 (2024). https://doi.org/10.1002/advs.202308561
14. Liu, B. et al. Bian, 4D printed hydrogel scaffold with swelling-stiffening properties and programmable deformation for minimally invasive implantation. *Nat. Commun.* **15** (1), 1587 (2024).
15. Deng, C. et al. 4D printing of magnetic smart structures based on light-cured magnetic hydrogel. *Chemical Engineering Journal* **494**, 152992 (2024). https://doi.org/10.1016/j.cej.2024.152992
16. Li, S. et al. J. Fu, 4D printing of biomimetic anisotropic self-sensing hydrogel actuators, Chemical Engineering Journal 473 145444. (2023).
17. Chen, L. et al. Thermal-responsive hydrogel surface: tunable wettability and adhesion to oil at the water/solid interface. *Soft Matter*. **6** (12), 2708–2712 (2010).
18. Lopez-Larrea, N. et al. PNIPAM/PEDOT: PSS Hydrogels for Multifunctional Organic Electrochemical Transistors, Advanced Functional Materials 2403708. (2024).
19. Liu, J., Jiang, L., He, S., Zhang, J. & Shao, W. Recent progress in PNIPAM-based multi-responsive actuators: A mini-review. *Chem. Eng. J.* **433**, 133496 (2022).
20. Sanzari, I. et al. Poly (N-isopropylacrylamide) based thin microgel films for use in cell culture applications. *Sci. Rep.* **10** (1), 6126 (2020).
21. Khumngern, S. & Jeerapan, I. Synergistic convergence of materials and enzymes for biosensing and self-sustaining energy devices towards on-body health monitoring. *Commun. Mater.* **5** (1), 135 (2024).
22. Goo, B., Hong, C. H. & Park, K. 4D printing using anisotropic thermal deformation of 3D-printed thermoplastic parts. *Mater. Design*. **188**, 108485 (2020).
23. Bodaghi, M., Damanpack, A. & Liao, W. Adaptive metamaterials by functionally graded 4D printing. *Mater. Design*. **135**, 26–36 (2017).
24. Van Manen, T., Janbaz, S. & Zadpoor, A. A. Programming 2D/3D shape-shifting with hobbyist 3D printers. *Mater. Horiz.* **4** (6), 1064–1069 (2017).
25. Kaehr, B. & Shear, J. B. Multiphoton fabrication of chemically responsive protein hydrogels for microactuation, Proceedings of the National Academy of Sciences 105(26) 8850–8854. (2008).
26. Ji, Q. et al. 4D Thermomechanical metamaterials for soft microrobotics, 2(1) 1–6. (2021).
27. Erb, R. M., Sander, J. S., Grisch, R. & Studart, A. R. Self-shaping composites with programmable bioinspired microstructures. *Nat. Commun.* **4** (1), 1712 (2013).
28. Decroly, G. et al. A Voxel-Based approach for the generation of advanced kinematics at the microscale. *Adv. Intell. Syst.* **5** (7), 2200394 (2023).
29. Spratte, T. et al. Selhuber-Unkel, increasing the efficiency of thermoresponsive actuation at the microscale by direct laser writing of pNIPAM. *Adv. Mater. Technol.* **8** (1), 2200714 (2023).
30. Zheng, C. et al. Light-driven micron-scale 3D hydrogel actuator produced by two-photon polymerization microfabrication. *Sens. Actuators B*. **304**, 127345 (2020).
31. Tao, Y. et al. Monolayer heterojunction interactive hydrogels for high-freedom 4D shape reconfiguration by two-photon polymerization. *Int J Bioprint* **9**, 678 (2023). https://doi.org/10.18063/ijb.678
32. Barwig, C. et al. Two-Photon Direct Laser Writing of pNIPAM Actuators in Microchannels for Dynamic Microfluidics. *Advanced Intelligent Systems* **6**, 2300829 (2024). https://doi.org/10.1002/aisy.202300829
33. van Altena, P. F. & Accardo, A. Micro 3d printing elastomeric ip-pdms using two-photon polymerisation: A comparative analysis of mechanical and feature resolution properties. *Polymers* **15** (8), 1816 (2023).
34. Mogas-Soldevila, L. et al. Driving macro-scale transformations in three-dimensional-printed biopolymers through controlled induction of molecular anisotropy at the nanoscale. *Interface Focus*. **14** (3), 20230077 (2024).
35. Xu, S., Wu, S., Zhu, R., Qiu, Z. & Yan, Y. Fully Physically Crosslinked PNIPAM Ionogels with High Mechanical Properties and Temperature-Managed Adhesion Achieved by H2O/Ionic Liquid Binary Solvents. *Advanced Functional Materials* **34**, 2405965 (2024). https://doi.org/10.1002/adfm.202405965
36. Rana, M. M. De La Hoz siegler, tuning the properties of PNIPAm-based hydrogel scaffolds for cartilage tissue engineering. *Polymers* **13** (18), 3154 (2021).

37. Han, D., Lu, Z., Chester, S. A. & Lee, H. Micro 3D printing of a temperature-responsive hydrogel using projection micro-stereolithography, Scientific reports 8(1) 1963. (2018).
38. Brinson, H. F. & Brinson, L. C. *Polymer Engineering Science and Viscoelasticity* (Springer, 2008).
39. Holzapfel, G. A. *Nonlinear Solid Mechanics: a Continuum Approach for Engineering Science* (Kluwer Academic Publishers Dordrecht, 2002).
40. Selby, A., Maldonado-Codina, C. & Derby, B. Influence of specimen thickness on the nanoindentation of hydrogels: measuring the mechanical properties of soft contact lenses. *J. Mech. Behav. Biomed. Mater.* **35**, 144–156 (2014).
41. Hu, Y. et al. Botanical-inspired 4D printing of hydrogel at the microscale. *Adv. Funct. Mater.* **30** (4), 1907377 (2020).
42. Zheng, J. et al. W.J. Li, 4D Printed Soft Microactuator for Particle Manipulation via Surrounding Medium Variation, Small 2311951. (2024).
43. Tao, Y. et al. Four-Dimensional Stimuli-Responsive Hydrogels Micro-Structured via *Femtosecond Laser Additive Manuf.*, **13**(1) 32. (2021).
44. Liu, X. et al. *Capillary-Force-Driven Self-Assembly 4D-Printed Microstructures* **33**(22), 2100332 (2021).
45. Huang, T. Y. et al. H.J.S.a. Duan, Four-dimensional micro-building blocks, 6(3) eaav8219. (2020).
46. Qu, J., Kadic, M., Naber, A. & Wegener, M. Micro-Structured Two-Component 3D Metamaterials with Negative Thermal-Expansion Coefficient from Positive Constituents. *Sci Rep* **7**, 40643 (2017). https://doi.org/10.1038/srep40643
47. Mourran, A., Zhang, H., Vinokur, R. & Möller, M. J. A. M. *Soft Microrobots Employing Nonequilibrium Actuation Via Plasmonic Heat.*, **29**(2) 1604825. (2017).
48. Zadpoor, A. A. Meta-biomaterials. *Biomaterials Sci.* **8** (1), 18–38 (2020).
49. Lee, Y. Y., Kim, R. M., Im, S. W., Balamurugan, M. & Nam, K. T. Plasmonic metamaterials for chiral sensing applications. *Nanoscale* **12** (1), 58–66 (2020).
50. Mirzaali, M. J., Pahlavani, H., Yarali, E. & Zadpoor, A. Non-affinity in multi-material mechanical metamaterials. *Sci. Rep.* **10** (1), 11488 (2020).
51. Andolfi, L. et al. Scanning probe microscopies: imaging and biomechanics in reproductive medicine research. *Int. J. Mol. Sci.* **22** (8), 3823 (2021).

Author contributions

E.Y., A.M., and K.C. conducted the experiments. E.Y. drafted the manuscript. V.M. performed the numerical modeling. L.v.Z. contributed to the nanoindentation experiments. A.A.Z., A.A., and M.J.M. supervised the study and reviewed the manuscript. All authors contributed to manuscript revision and approved the final version.

Funding

This work was supported by the Cohesion grant "Biomimetic-meta-implants" awarded to M.J.M. and A.A.

Declarations

Competing interests

The authors declare that they have no known competing financial interests or personal relationships that could have appeared to influence the work reported in this paper.

Additional information

Supplementary Information The online version contains supplementary material available at https://doi.org/10.1038/s41598-025-06269-2.

Correspondence and requests for materials should be addressed to E.Y., A.A. or M.J.M.